

Implementation of a local principal curves algorithm for neutrino interaction reconstruction in a liquid argon volume

J.J. Back^{a,1}, G.J. Barker¹, S.B. Boyd¹, J. Einbeck², M. Haigh¹, B. Morgan¹, B. Oakley¹, Y.A. Ramachers¹, D. Roythorne¹

¹Department of Physics, University of Warwick, Coventry CV4 7AL, UK

²Department of Mathematical Sciences, Durham University, Durham DH1 3LE, UK

Received: 23 December 2013 / Accepted: 19 March 2014

Abstract A local principal curve algorithm has been implemented in three dimensions for automated track and shower reconstruction of neutrino interactions in a liquid argon time projection chamber. We present details of the algorithm and characterise its performance on simulated data sets.

1 Introduction

Liquid argon time projection chambers (LAr-TPCs), that are currently in development in various R&D programmes in Europe, Japan and the USA [1], are acknowledged to be a detector technology capable of meeting the physics requirements of a next-generation neutrino oscillation experiment. They can provide simultaneous tracking and calorimetry of particles from neutrino interactions over a wide range of energies, with exquisite millimetric granularity, as demonstrated by results from ICARUS [2]. Despite this advantage, it has proven difficult to achieve an automated software process that can fully reconstruct neutrino interactions, which will contain a mixture of ionisation tracks as well as electromagnetic and hadronic showers, especially when the neutrino interaction point is not known beforehand. In this paper, we describe a first application of using local principal curves [3] to automatically reconstruct neutrino interactions using three-dimensional LAr-TPC data.

When a charged particle passes through a liquid argon medium it releases a stream of ionisation charge which can be measured by a TPC to provide a 3D trajectory in space. We can represent this data as a collection of “hits”, each of which contain the spatial cell co-ordinate information (x, y, z) as well as the charge or

energy deposit Q . The task of any reconstruction algorithm is to first obtain the hits from the detector output, then group these hits into clusters in order to identify the particles coming from the neutrino interaction, before extracting physics parameters such as momentum or energy from the reconstructed particles. Here, the first stage of the analysis chain, hit reconstruction, is assumed to have already taken place and the input is taken to be the complete set of hits in three spatial dimensions. Our reconstruction algorithm takes the collection of hits for each neutrino interaction (labelled as an event) and forms clusters of associated hits in order to identify the particles. The mathematics and logic behind the local principal curve procedure is described in Sect. 2, while a description of the simulation methods used to obtain samples of neutrino interaction events in liquid argon is given in Sect. 3. The performance of the reconstruction algorithm is discussed in Sects. 4 and 6, with details about using it for track-shower discrimination provided in Sect. 5. Finally, we summarise our findings in Sect. 7.

2 The local principal curve (lpc) algorithm

The key component of the method we are proposing is the mean shift procedure, a versatile tool which is popular mainly in the computer vision community [4]. In essence, the mean shift moves a point to the local mean of the data around this point. For our case, the points are the positions $X_i(x, y, z)$ of all of the hits, which are each scaled by their range, defined to be the difference between the largest and smallest values of X_i (though it is also possible not to scale at all, or to scale by other measures of spread such as the standard

^ae-mail: j.j.back@warwick.ac.uk

deviation). The local mean $m(u)$ for a set of N hits is defined as

$$m(u) = \frac{\sum_{i=1}^N w_i(u) X_i}{\sum_{i=1}^N w_i(u)}, \quad (1)$$

where the weights $w_i(u)$, which determine the size and shape of the local neighbourhood at a chosen location u , are monotonically decreasing with increasing distance from u to X_i . A common choice of weights is the Gaussian density function

$$w_i(u) = \frac{Q_i}{(2\pi)^{3/2} h^3} \exp \left\{ -\frac{1}{2h^2} (X_i - u)^T (X_i - u) \right\}, \quad (2)$$

where Q_i is the energy deposit for hit i and h is a constant bandwidth parameter that steers the size of the local neighbourhood. The weights play the role of “kernel” functions and can, if desired, be replaced by other functions such as a triangular-shaped or truncated probability density. In our scenario, where the co-ordinates are all measured on the same scale, we keep the Gaussian form and use the same bandwidth parameter for all three directions. The value of h can be selected through a coverage measure [3], though for our purposes there is not much reason for this, as roughly the same bandwidth, $h \sim 0.05$ after scaling, will be usable in a wide range of liquid argon detectors. Note that the normalisation denominator $(2\pi)^{3/2} h^3$ can be left out of the kernel function since it is a constant common factor for all hit points and has no effect on the properties of the principal curve.

From Eq. 1, we define the *mean shift* as

$$s(u) = m(u) - u = \frac{\sum_{i=1}^N w_i(u) (X_i - u)}{\sum_{i=1}^N w_i(u)}. \quad (3)$$

This quantity has many interesting properties [4], one of which being that $s(u) \propto \nabla \hat{f}(u) / \hat{f}(u)$, where $\hat{f}(u) = \frac{1}{N} \sum_{i=1}^N w_i(u)$ is a density estimate of f at u . This implies that the mean shift is a vector pointing into a denser direction of the data space. When carried out iteratively, starting at $u = m_0$, one can show [4] that the series of local means

$$m_{\ell+1} = m_\ell + s(m_\ell), \quad \ell \geq 0, \quad (4)$$

converges to a local mode u_m of $\hat{f}(u)$ where $s(u_m) = 0$. This has the attractive property of being a clustering technique; a trajectory can be formed by running the mean shift procedure on each data point X_i iteratively until convergence is achieved.

Though the convergence towards a local mode of the density is an appealing property, it has the negative side effect of getting trapped at the local modes and will not move beyond them. Therefore, some modification of Eq. 4 is needed which ensures that particle

trajectories are pursued beyond local modes. The simple idea is to alternate the mean shift with a local principal component step [3]. More specifically, let $\gamma(u)$ be the normalised eigenvector corresponding to the largest eigenvalue of the local symmetric 3×3 covariance matrix

$$\Sigma(u) = \frac{\sum_{i=1}^N w_i(u) (X_i - m(u))(X_i - m(u))^T}{\sum_{i=1}^N w_i(u)}. \quad (5)$$

Starting from a given point $u = m_0$, we set $\ell = 0$ and iterate between

1. computing the local centre of mass:

$$m(u_\ell) \equiv u_\ell + s(u_\ell); \quad (6)$$

2. finding the next local neighbourhood location:

$$u_{\ell+1} = m(u_\ell) + t \times \gamma_\ell, \quad (7)$$

where t is a given step size (of the same order as h) and $\gamma_\ell \equiv \gamma(u_\ell)$. The local principal curve is then defined as the series of local centres of mass $m(u_\ell)$. In our case, the starting point $u = m_0$ is chosen to be the position of the nearest hit to the energy-weighted centroid of all of the hits. Alternatively, m_0 can be set either at random from the X_i points, set by hand, or be chosen to be a local density mode using an initial mean shift procedure as outlined in Refs. [3, 5]. The above iteration is repeated until either the required number of lpc points (N_p) is obtained, or the path length along the local curve is no longer increasing (convergence).

As we will see later, the angle ϕ between the normalised eigenvector γ_ℓ and the preceding eigenvector $\gamma_{\ell-1}$ can be used to infer the presence of feature points, corresponding to drops in the angle profile along the principal curve, which provide evidence for particle decays or possible interactions between particles.

In order to provide inertia for reducing the chance of the local principal curve deviating too much from the general direction of neighbouring points, γ_ℓ is multiplied by an angle penalisation term $a = |\cos\phi|^\alpha$, where α is usually set to 2, when the next local neighbourhood location is found using Eq. 7:

$$\gamma_\ell := a\gamma_\ell + (1 - a)\gamma_{\ell-1}. \quad (8)$$

A technicality to be mentioned is that, for a given $\Sigma(u)$, the first eigenvector may equally well be $-\gamma(u)$ as well as $\gamma(u)$, so for each $\ell \geq 1$, one needs to check whether $\cos\phi > 0$ and set $\gamma_\ell := -\gamma_\ell$ otherwise [3].

Based on asymptotic considerations [5], it can be shown that the sequence of lpc points $m(u_\ell)$ converges to a point u_b close to the boundary of the cloud of data points with the property $f(u_b) = h|\nabla \hat{f}(u_b)|$. In practical terms, convergence is reached when the cumulative path length difference between neighbouring local curve

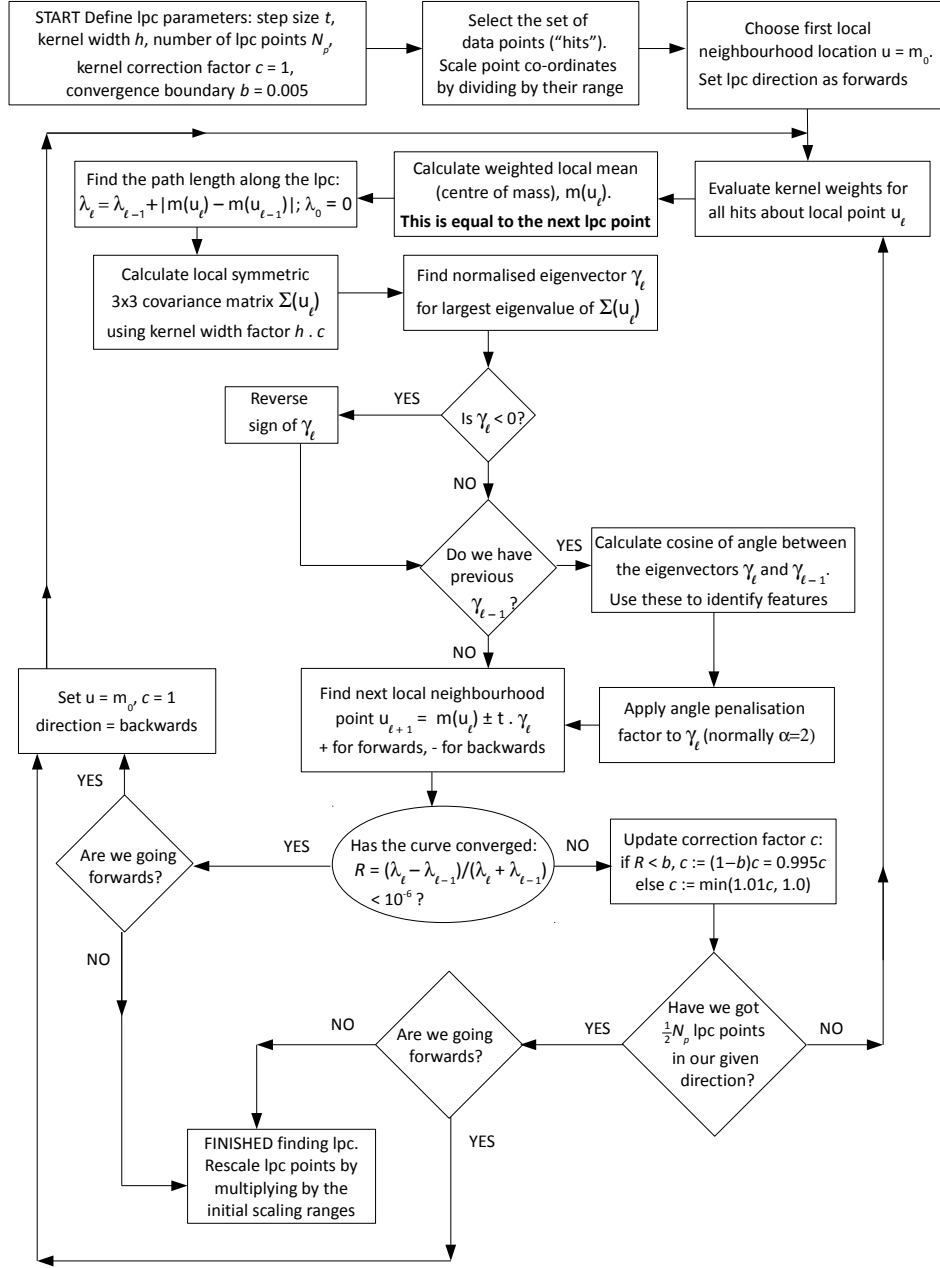


Fig. 1 Logic flow of the local principal curve (lpc) algorithm. The starting point is at the top left and the arrows show the direction to the next action (rectangle) or decision (diamond or ellipse)

points, divided by their sum, is below a chosen threshold typically set at 10^{-6} :

$$R = \frac{\lambda_\ell - \lambda_{\ell-1}}{\lambda_\ell + \lambda_{\ell-1}} < 10^{-6}, \quad (9)$$

where $\lambda_\ell = \lambda_{\ell-1} + |m(u_\ell) - m(u_{\ell-1})|$ and $\lambda_0 = 0$. In order to pick up features that may be present in the tails of the point cloud, convergence is delayed by multiplying the kernel bandwidth h with a correction factor c if R is below a certain boundary limit b , which is typically set to be 5×10^{-3} (which must be larger

than the threshold for R defined in Eq. 9). Initially, c is set to unity, but when $R < b$, c is reduced by the factor $(1 - b)$, and h in Eq. 2 needs to be replaced by $h \times c$. If $R \geq b$, then c is increased by 1% but must not exceed unity. After convergence, or after we have obtained $\frac{1}{2}N_p$ lpc points, the algorithm has to be restarted with $u = m_0$ in order to cover the other side of the data cloud, where the next neighbourhood location is defined as

$$u_{\ell+1} = m(u_\ell) - t \times \gamma_\ell, \quad (10)$$

and the lpc algorithm continues as usual.

Note that the cumulative path lengths λ_ℓ form a discrete parameterisation of the principal curve, which can be refined via a cubic spline interpolation towards a continuous parametrisation if necessary [6]. This can be useful since it allows the option to plot, and regress, physical quantities such as the amount of deposited energy as a function of distance along the particle trajectory covered by the local principal curve.

Figure 1 summarises the complete logic flow of the lpc algorithm. Once the lpc points are found, they are scaled-up using the initial co-ordinate ranges of the hits. The important parameters with suggested (scaled) values are given in Table 1. These parameters are optimised to provide the best overall reconstruction performance for specific classes of neutrino interaction events described in Sects. 4 and 6.

Table 1 Default parameters for the lpc algorithm

Kernel bandwidth factor h	0.05
Neighbourhood step size t	0.05 ($t \sim h$)
Number of lpc points N_p	100 to 200
Initial kernel bandwidth correction c	1
Angle penalisation factor α	2
Convergence boundary limit b	0.005
Convergence criteria threshold R	10^{-6}

3 Simulation of neutrino interactions in liquid argon

In order to test the reconstruction performance of the local principal curve algorithm for neutrino interaction events, the Geant4 simulation toolkit [7] was used to implement a model of a LAr-TPC detector, defined to be a stainless steel cylinder with height and radius both equal to 10 m centred at the origin (0,0,0) and filled with liquid natural argon. Particles are tracked through the detector volume with all electromagnetic and hadronic processes enabled. The “QGSP_BIC_HP” physics list is used to model the hadronic interactions, combining a quark-gluon string and binary cascade model with high precision low-energy (below 20 MeV) neutron cross-section data. The detector is divided into “voxels” with volumes equal to $(1 \times 1 \times 1) \text{ mm}^3$, and all primary and secondary particles are tracked through these down to an energy of 10 keV or until they leave the TPC volume. Energy deposits by charged particles passing through the voxels are tallied into a map between the co-ordinates of the centres of each voxel (x, y, z) and the total deposited energy (charge) Q . To take into account the effect of electron-ion recombination on the particle stop-

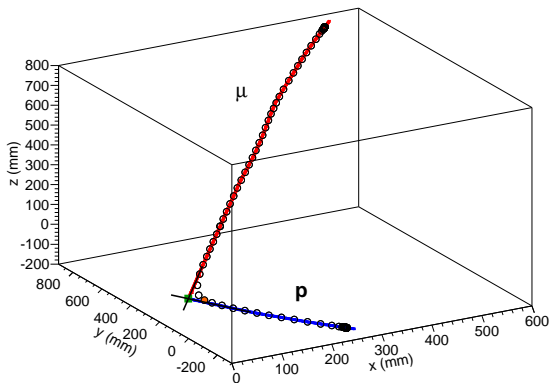
ping power in liquid argon, a quenching factor is applied to all deposited energies using a modified form of Birks’ law according to results obtained from the ICARUS project [8]. No attempt is made to model the detector readout system since this is highly experiment-specific. The GENIE [9] package is used to simulate the primary particles from muon-neutrino and electron-neutrino interactions with a monoenergetic spectrum at 0.77 GeV, which corresponds to the JPARC neutrino beam mean energy. The neutrinos are directed in a beam along the x -axis through the centre (0,0,0) of the detector. In order to remove random hits from secondary low-energy interactions, an initial filtering is applied to all of the hits using a density-based spatial clustering algorithm [10,11]. Hits are required to be part of density-connected regions which contain at least 10 hits, whereby the maximum allowed distance between a hit and its nearest neighbour is 2 cm. Excluded hits are classified as “noise” and are removed from further processing.

4 Charged-current quasi-elastic interactions:

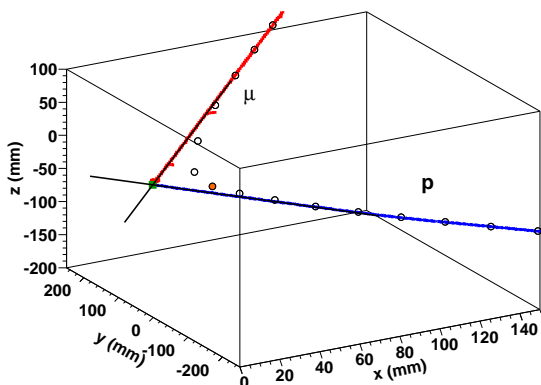
$$\nu_\mu + n \rightarrow \mu + p$$

The suitability of using the local principal curve algorithm to reconstruct neutrino interactions can be demonstrated by its ability to identify muon-neutrino charged-current quasi-elastic (CCQE) events, which have a simple two-track topology involving a short proton track and a long muon track originating from a common primary vertex point, with variable opening angle. Figure 2 shows an example reconstruction of a 770 MeV muon-neutrino to muon-proton event, where it can be clearly seen that the calculated points on the curve follow the hits closely. Along the middle portions of each track, the lpc points are roughly equidistant from each other, which is an indication that the neighbouring hits are essentially along a straight line. At the end of each track, the lpc points begin to clump together as they approach convergence.

Near the primary vertex position, the curve points transfer from the muon track onto the proton track. During this transition, the angle ϕ between the eigenvectors of neighbouring lpc points increases. As shown in Fig. 3, plotting the distribution $1 - |\cos\phi|$ as a function of lpc point number (or alternatively as a function of the cumulative path length λ_ℓ) will produce a peak that will identify the specific lpc *feature point* ℓ_f which has the largest angle ϕ , and can be used to reconstruct the interaction vertex. First, we ignore the two lpc points on either side of the feature point, since the local curve is still rapidly changing direction, and only consider the points numbered between ℓ_{f+2}, ℓ_{f+4}



(a)



(b)

Fig. 2 An example lpc reconstruction of a muon-proton event showing the hits associated to the muon (red) and proton (blue) tracks together with the calculated lpc points (open circles). Also shown are the two line segments used to find the position of the primary interaction vertex (green square). These lines are made from hits on either side of the feature point of the principal curve, which has the largest $1 - |\cos\phi|$ value, and is shown as an orange-filled circle. Plot (b) is a close-up view of the interaction region of plot (a)

on one side and ℓ_{f-4}, ℓ_{f-2} on the other side. Additionally, any other feature points (with lower $1 - |\cos\phi|$ peaks) that may exist between ℓ_{f-4} and ℓ_{f+4} are ignored and are considered to be just part of the original feature point ℓ_f . For each range, straight lines are fitted to the hits that are closest to the lpc points. Each line is defined as a single point, taken to be the centroid of the nearby hits, and a direction, which is chosen to minimise the sum of the perpendicular Euclidean distances of each hit to the line. Next, an initial value of the vertex position, which will have a typical resolution of approximately 1 cm, is taken to be the point of closest approach between the two straight line sections. The reconstruction precision of the vertex location can be sig-

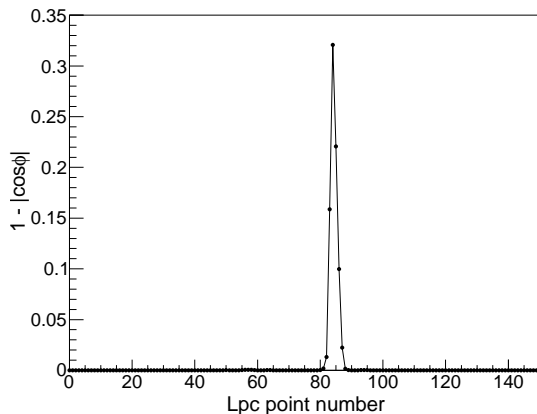


Fig. 3 Graph showing the quantity $1 - |\cos\phi|$, for the example muon-proton event shown in Fig 2, for points along the principal curve, where ϕ is the angle between the eigenvector γ_ℓ and the preceding eigenvector $\gamma_{\ell-1}$ for lpc point ℓ . The feature point is identified as the peak

nificantly improved by extending the straight lines towards the direction of the initial vertex point by adding hits that are closest to a given line. These additional hits improve the accuracy of the new centroid and direction of the two straight lines. The vertex position is then taken to be the point of closest approach to these extended lines, leading to an improved resolution of approximately 1.5 mm. It is important to emphasise that the above method can only reliably reconstruct two-prong vertices.

Figure 4 shows the distributions of the primary vertex position in x , y and z for a sample of 770 MeV neutrino to muon-proton events when the proton track has a minimum number of 25 hits (equal to a range of 2.5 cm), which is roughly equivalent to an energy threshold of 10 MeV for a minimum ionising particle in liquid argon. Approximately $15 \pm 1\%$ of protons from a sample of $\nu_\mu + n \rightarrow \mu + p$ events will not satisfy this minimum range requirement. The vertex distributions are fitted to double Gaussian functions, which are defined to be the sum of two Gaussians having the same mean μ but different widths σ_1 and σ_2 , with relative amplitude r . The resolution of the vertex position in each co-ordinate direction is taken to be the effective width of the corresponding double Gaussian fit $\sigma_{\text{eff}} = \sigma_1 + r\sigma_2$. As mentioned previously, the neutrino beam direction is defined to be along the x axis, and so the muon and proton tracks originating from the vertex will tend to have their largest momentum component along x . This has the effect of producing a very slight positive bias (0.32 ± 0.05 mm) for the determination of the x position of the vertex point when using the above extended straight line method. Theoretically, this bias could be reduced by having a smaller step size so that the princi-

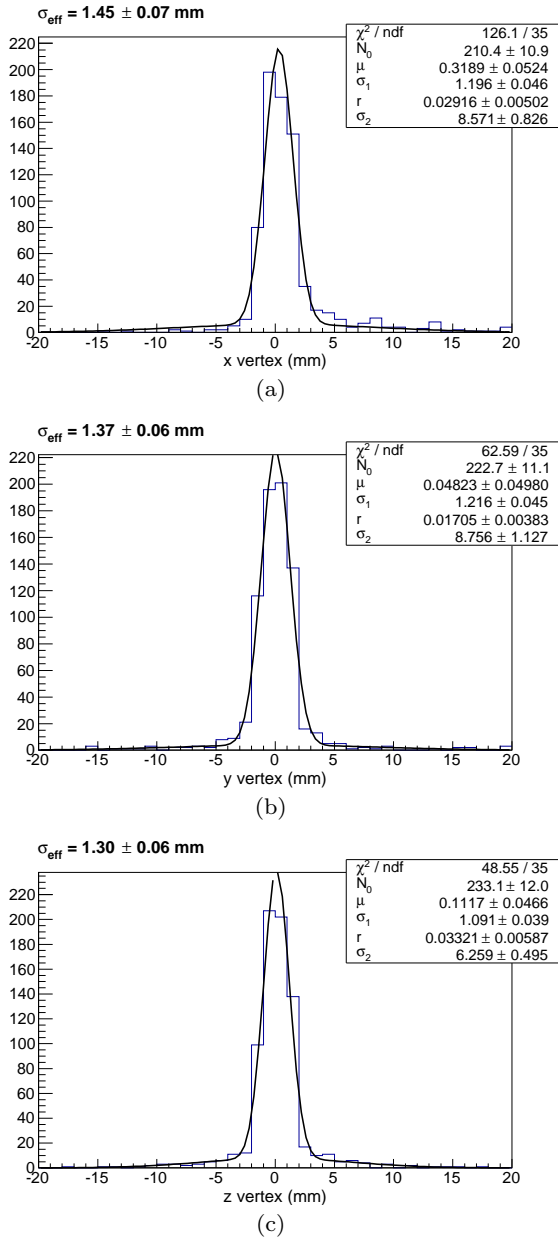


Fig. 4 Double Gaussian fits to the distributions of the reconstructed primary vertex position in x , y and z for muon-proton events that satisfy the proton range requirement. Approximately 90% of these events have a primary vertex found within 2 cm from the true vertex position $(0,0,0)$

pal curve can get closer to the hits in the primary vertex region. In practice, this does not significantly improve the overall vertexing performance, since reducing the step size has the effect of increasing the occurrence of fake secondary vertices (i.e. multiple $1 - |\cos\phi|$ peaks), since the algorithm becomes more susceptible to fluctuations in the hit point cloud. As illustrated by Fig. 5, approximately 90% of the events that pass the proton

range selection have a primary vertex found within 2 cm from the generated position $(0,0,0)$.

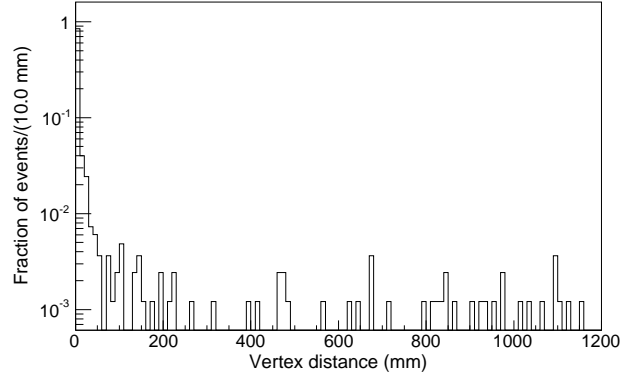


Fig. 5 The distribution of the distance of the reconstructed primary vertex position from the generated position $(0,0,0)$ for muon-proton events that pass the range selection on the proton track

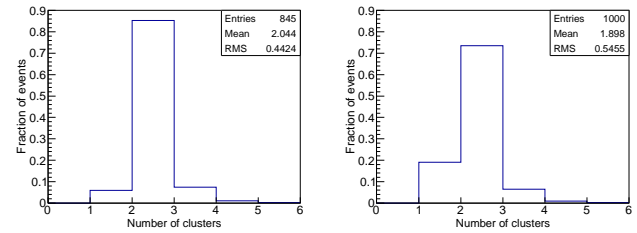


Fig. 6 The distribution of reconstructed clusters in a sample of 1000 muon-proton events for (left) events passing a range selection on the proton track and (right) with no range requirement imposed

Once a primary vertex has been found, it is then possible to assign the hits on each extended straight line section to be the start of separate *clusters* for the proton and muon track. Further hits are added to each cluster by continuing along the principal curve direction initially given by the straight line section and adding hits that are closest to the remaining lpc points. Figure 6 shows the number of clusters found in muon-proton events with and without the proton range requirement. Most events have just two clusters reconstructed, as expected, although about 6% of the events only have one cluster found, which occurs when the proton track has been missed, i.e. the hits are just assigned to be the muon, and the vertex point is taken to be just the start of the muon track. More single cluster events (about 19%) are reconstructed when no proton range selection is imposed. For about 10% of the events, more than two clusters are found, which occurs when

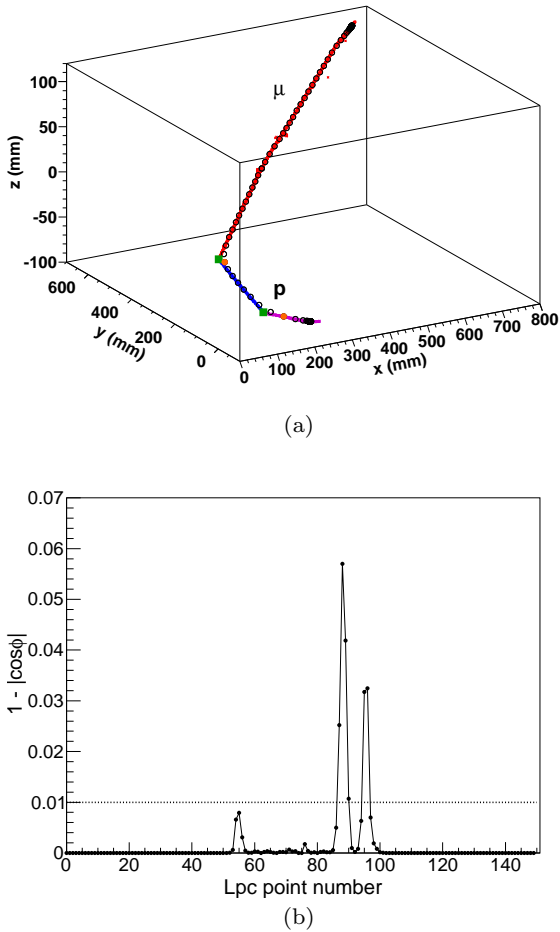


Fig. 7 An example lpc reconstruction of a muon-proton event where the proton has been hard scattered. Image (a) shows the hits associated to the muon (red) and proton (pre-scatter in blue, post-scatter in magenta) tracks. Also shown are the calculated lpc points (open circles) and feature points of the principal curve (orange-filled circles), together with the reconstructed primary and secondary interaction vertices (green squares). The feature points are those that correspond to the peaks in the $1 - |\cos\phi|$ distribution shown in plot (b); these peaks are above the selection limit value of 0.01 represented by the dotted horizontal line

two or more feature points are present with $1 - |\cos\phi|$ values above the threshold value of 0.01, which was chosen based on observations of the typical heights of the feature peaks. Most of these additional secondary vertices, which are reconstructed using the same two-line method described earlier, have genuine physics reasons: the proton or muon track scatters off a nucleus such as that shown in Fig. 7, or the muon decays to a low energy electron, producing a short two-prong stub at the end of the muon track. To reduce the chance of incorrectly finding secondary vertices, neighbouring clusters that have principal axes within 20 degrees from each other are merged and considered to be just one cluster, and

the secondary vertex between them is removed. Varying this merging angle did not significantly improve the overall reconstruction performance. When more than one vertex is found, the vertex with the lowest x coordinate is chosen to be the primary vertex, since the neutrino beam is directed along the positive x direction. Note that the earlier primary vertex resolution plots shown in Fig. 4 include events with secondary vertices found; only the vertex with the lowest x value is included in the fitted distributions.

An important measure of the performance of this reconstruction algorithm is how well it can correctly associate hits to each generated particle. The first figure of merit is known as the average cluster efficiency ϵ_c , which is equal to the number of reconstructed clusters which have the majority of the hits with the correct particle type divided by the number of events. This quantity is strongly correlated with the efficiency of finding a vertex, whereby the initial hit cloud is broken up into the separate particle tracks (clusters). The second figure of merit is the hit efficiency ϵ_h for each cluster, defined to be the ratio of correct hits associated to the cluster compared to all hits produced by the original particle. Therefore, the overall efficiency of reconstructing a given particle is equal to the product of the cluster and hit efficiencies. Furthermore, the hit purity ϵ_p is defined to be the fraction of hits in a given reconstructed cluster that have the correct particle type.

The parameters of the principal curve defined in Table 1 were optimised in order to give, on average, two clusters per muon-proton event, as well as providing maximal cluster and hit efficiencies and purities for the reconstructed muon and proton tracks. The only parameters that can significantly affect the performance in this regard are the kernel width h , the step size t and the number of lpc points N_p (the other parameters are left unchanged). Table 2 shows the results from this optimisation. It was found that variations to the kernel width and step size within the range 0.04 to 0.06 did not significantly affect the reconstruction performance, and using between 100 and 300 lpc points also produced similar results.

5 Shower and track discrimination

We have seen that the principal curve algorithm has a very good performance for reconstructing muon-neutrino CCQE events. We next tested whether the algorithm can infer the presence of electron-neutrinos via the interaction $\nu_e + n \rightarrow e + p$, which means identifying electron showers and proton tracks originating from a common vertex with variable opening angle. Before this can

Table 2 Optimised performance of the lpc algorithm for 770 MeV neutrino to muon-proton events that satisfy the proton range requirement (845 out of an initial sample of 1000). Efficiencies and purities are averaged over all selected events

Quantity	Value
Lpc scaled kernel bandwidth h	0.056
Lpc scaled step size t	0.040
Number of lpc points	150
Fraction of events with no vertex found	5.9 ± 0.8 %
Muon cluster efficiency	99.5 ± 0.2 %
Muon hit efficiency	93.7 ± 0.8 %
Muon reconstruction efficiency	93.2 ± 0.9 %
Muon hit purity	98.5 ± 0.4 %
Proton cluster efficiency	93.5 ± 0.08 %
Proton hit efficiency	91.7 ± 0.9 %
Proton reconstruction efficiency	85.8 ± 1.2 %
Proton hit purity	97.3 ± 0.6 %
Vertex efficiency within ± 2 cm	89.9 ± 0.6 %
Vertex x position resolution	1.45 ± 0.07 mm
Vertex y position resolution	1.37 ± 0.06 mm
Vertex z position resolution	1.30 ± 0.06 mm

be attempted, we first need to implement a set of selection criteria that can tell us whether a cluster is either a shower or a track. This can be achieved by looking at the differences between the transverse and longitudinal extent of clusters. To avoid overcomplicating the track-vs-shower analysis, only one principal curve is found per generated particle, and no vertex finding nor division into sub-clusters is performed. As shown in Fig. 8, an electron shower will generally produce a halo of hits that surround the principal axis of the point cloud, whereas a track will essentially be a continuous line of hits with slight changes in direction owing to the effects of multiple scattering. These topological differences can be quantified by looking at the Euclidean distance of each hit from its nearest calculated lpc point. These are known as *residuals*, labelled as δr , and are a measure of the transverse extent of the hits in a cluster; in general, showers will have larger residuals.

Figure 9 shows the distribution of hit-to-principal-curve residuals for 1,000-event samples of single particle, monoenergetic (0.5 and 1.5 GeV) electrons and muons. In order to enhance the differences between tracks and showers, very small residuals are ignored, since they are present in both samples, and only the residuals $\delta r'$ that are larger than 30% of the maximum residual δr_{\max} in a given cluster are considered. This has the effect of producing a narrowly-peaked distribution with a longer tail on the high end for tracks, and a very broad, almost flat, distribution for showers. A possible selection criterion for discriminating between them is to require $\delta r'$ to be above the value where the electron distribution intersects the high-end tail of the muon distribution. For 0.5 GeV, the selec-

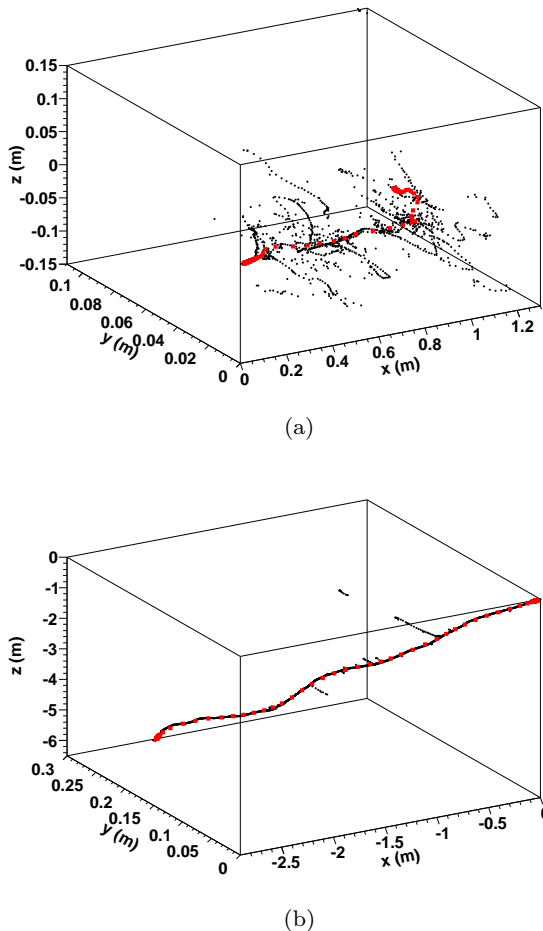
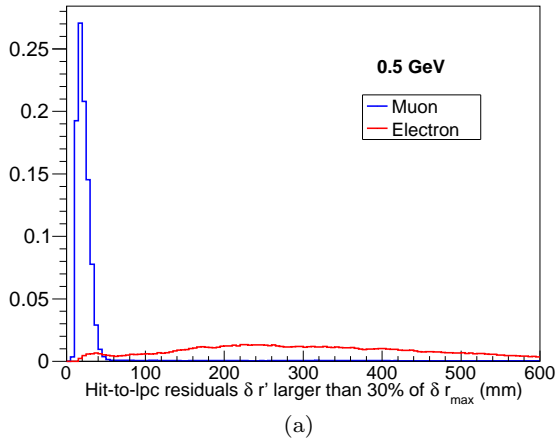
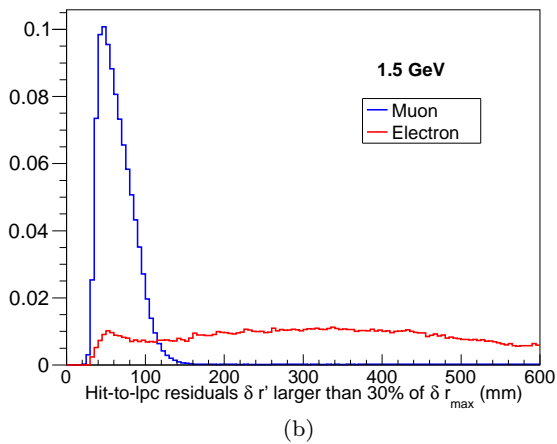


Fig. 8 Example principal curves (red squares) for 1.5 GeV (a) electron shower and (b) muon track with delta electrons

tion $\delta r' > 4$ cm will identify approximately 96% of electrons as showers and only 6% of muons as showers. At 1.5 GeV, the intersection value increases to $\delta r' = 12$ cm, degrading the shower identification efficiency to 86% for electrons, while slightly improving the muon shower misidentification probability to 3%. However, this selection criteria is energy dependent, meaning that the energy of the cluster needs to be known before a decision can be made as to whether the particle is a shower or a track. To avoid this difficulty, a common selection value is imposed on all clusters irrespective of their energy, namely that a shower must have at least 90% of its $\delta r'$ residuals to be longer than 2 cm. This gives a comparable performance to the energy-dependent selection for 0.5 GeV particles, but offers no discrimination power at 1.5 GeV or higher energies. This can be understood by looking at the example events shown in Fig. 8. For the muon, there are additional hit points that are perpendicular to the general direction of the track which originate from (delta) electrons that are



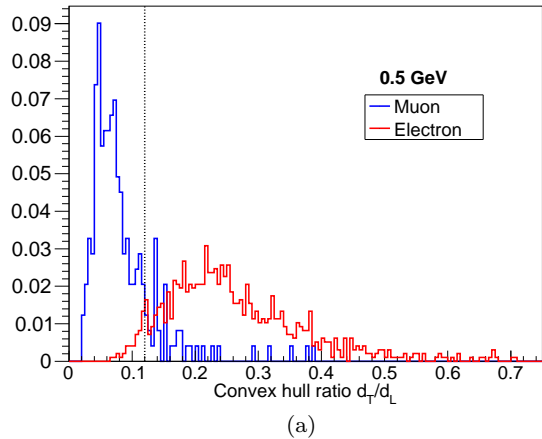
(a)



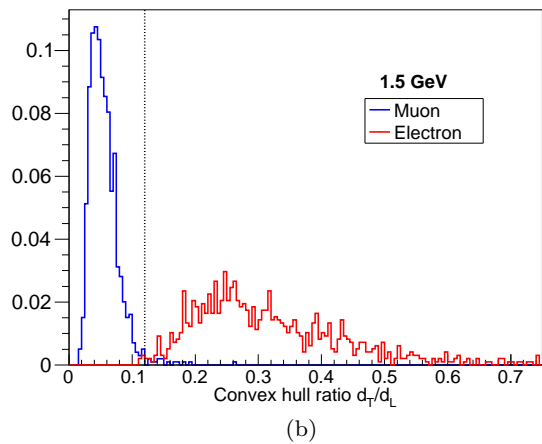
(b)

Fig. 9 Normalised distributions of the hit-to-lpc residuals $\delta r'$ for (a) 0.5 GeV and (b) 1.5 GeV muon tracks and electron showers. Here, $\delta r'$ denotes residuals that are larger than 30% of the value of the maximum residual δr_{\max}

knocked-off neighbouring atoms as the muon passes by. The residuals of these extra hits are large enough to be comparable to the typical residuals observed for electron showers. To remedy this problem, an additional variable is used, namely the ratio of the transverse-to-longitudinal extent d_T/d_L of a convex hull volume that defines the outer edge which encompasses all of the hits in the cluster [12]. Here, the longitudinal component d_L is defined to be the hull length along the principal axis of the cluster, while the transverse component d_T is the sum of the two lengths that are orthogonal to d_L . In general, showers will have larger convex hull ratios when compared to tracks. Figure 10 shows the distributions of this quantity for 0.5 and 1.5 GeV electrons and muons after the previously defined selections on the residuals $\delta r'$ have been applied. Track-shower discrimination at high energies is restored, with minimal impact on the performance at low energies, by requir-



(a)



(b)

Fig. 10 Normalised distributions of the convex hull ratio for (a) 0.5 GeV and (b) 1.5 GeV muon tracks and electron showers that have at least 90% of their hits with $\delta r'$ at least equal to 2 cm. The dotted vertical line represents the selection on the convex hull ratio; showers (tracks) have convex hull ratios above (at or below) 0.12

ing the convex hull ratio to be larger than 0.12 for all cluster energies, which corresponds to tracks having a length about 8 times longer than the transverse extent of any hit point filaments originating from delta electrons.

Table 3 Shower identification efficiencies for electron and muon monoenergetic particles based on 1,000-event samples

Generated energy (GeV)	Electron efficiency (%)	Muon efficiency (%)
0.5	94.7 ± 0.7	3.8 ± 0.6
1.0	98.4 ± 0.4	2.1 ± 0.5
1.5	99.5 ± 0.2	1.9 ± 0.4
2.0	99.8 ± 0.1	1.3 ± 0.4
2.5	99.9 ± 0.1	1.4 ± 0.4
3.0	100.0	0.9 ± 0.3

Table 3 provides a summary of the shower identification efficiencies for electrons and muons; a cluster is classified as a shower if at least 90% of the $\delta r'$ residuals are larger than 2 cm, and if it has a convex-hull ratio above 0.12. In fact, these selection requirements produce the optimal separation between tracks and showers based on the significance defined as $\epsilon_e/\sqrt{\epsilon_e + \epsilon_\mu}$, where ϵ_e (ϵ_μ) is the efficiency of identifying an electron (muon) as a shower. For the previous 770 MeV neutrino to muon-proton event sample discussed in Sect. 4, the probability of misidentifying muons (protons) as showers is $6.6 \pm 0.6\%$ ($7.9 \pm 0.6\%$), which is slightly worse than the expected value of approximately 4% owing to some of the original hits being left out of the reconstructed clusters (see the efficiencies in Table 2), which will affect the distributions of the residuals and convex-hull ratios.

6 Electron–proton neutrino interactions:

$\nu_e + n \rightarrow e + p$

We now have all of the ingredients to fully reconstruct electron-proton events, which have a two-prong topology involving a short proton track and an electron which initially starts off like a track but quickly produces a cascade of hits in the form of an electromagnetic shower, resulting in a halo of hits along the initial direction of the electron. Figure 11 shows an example 770 MeV electron-neutrino interacting with a neutron to produce an electron shower and proton track originating from a common vertex point. The calculated points of the principal curve follow the hits of the proton track closely. They then bend around the vertex region to follow the hits in the initial track-like segment of the electron, then continue along the principal axis of the shower until the end of the core region has been reached. The primary vertex is reconstructed using exactly the same extended two-line method that was used for muon-proton events in Sect. 4. As before, the main feature point (with $1 - |\cos\phi| > 0.01$) is used to find the extended straight line sections for the proton and track-like segment of the electron, and the reconstructed primary vertex corresponds to their point of closest approach. Then, two clusters are formed, one on each side of the vertex, from hits that are closest to these straight lines. Further hits are added to each cluster by continuing along the principal curve direction initially given by the straight line section and adding hits that are closest to the remaining lpc points that have δr residuals below 10 cm.

Figure 12 shows double Gaussian fits to the primary vertex position in x , y and z for a sample of 770 MeV neutrino to electron-proton events when the

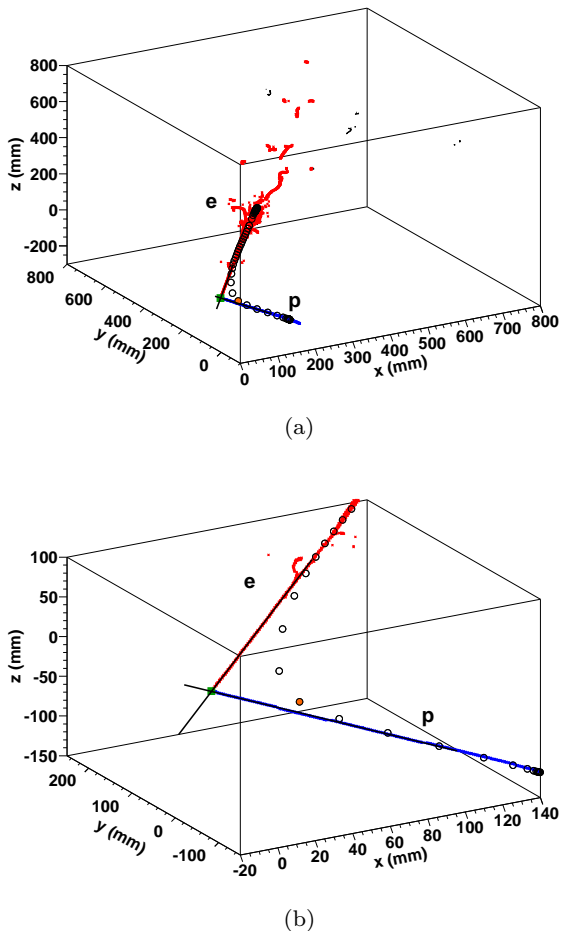


Fig. 11 An example lpc reconstruction of an electron-proton event showing the hits associated to the electron shower (red) and proton track (blue) together with the calculated lpc points (open circles). Also shown are the two line segments used to find the position of the primary interaction vertex (green square). These lines are made from hits on either side of the feature point of the principal curve, which has the largest $1 - |\cos\phi|$ value, and is shown as an orange-filled circle. Plot (b) is a close-up view of the interaction region of plot (a)

proton track has a minimum number of 25 hits. Approximately $15 \pm 1\%$ of protons in a sample of $\nu_e + n \rightarrow e + p$ events will not satisfy this hit requirement. The vertexing resolution, taken to be the effective width of the corresponding double Gaussian fit, is slightly worse than the resolution obtained for muon-proton events. This is to be expected, since the onset of the electromagnetic shower will produce hits that will be some distance away from the initial direction of the electron, affecting the accuracy of finding the extended line sections. As was the case for muon-proton events, the determination of the x position of the vertex point has a slight positive bias of 0.23 ± 0.06 mm. Despite the

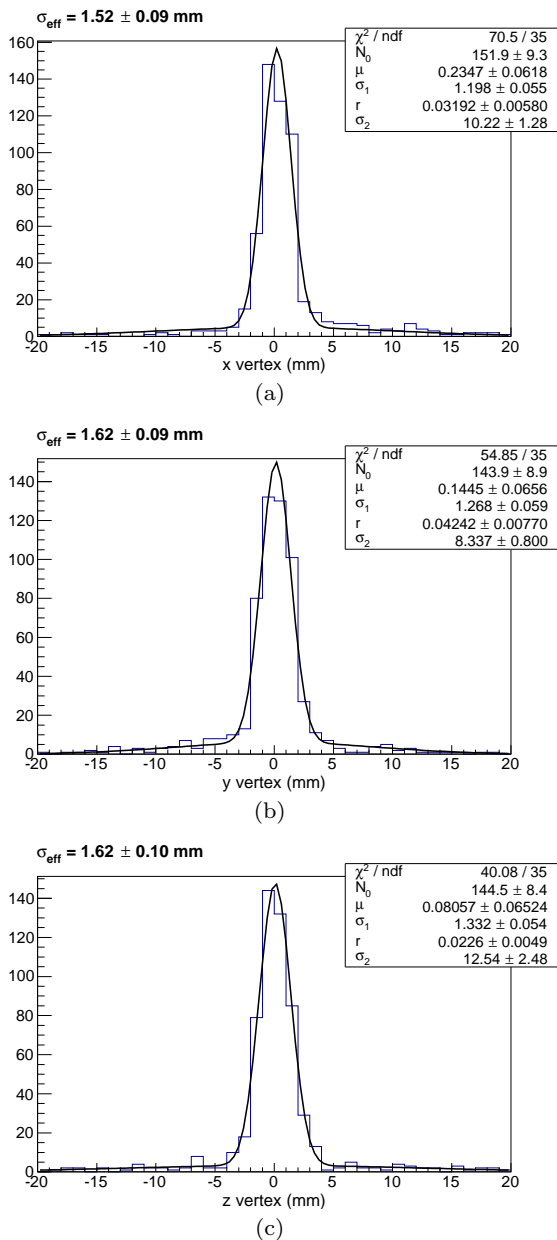


Fig. 12 Double Gaussian fits to the distributions of the reconstructed primary vertex position in x , y and z for electron-proton events. Approximately two-thirds of events have a primary vertex found within 2 cm from the true vertex position (0,0,0)

rather good vertex resolution of approximately 1.5 to 1.6 mm in each direction, only 67% of the events that pass the proton hit requirement have a vertex found within ± 2 cm from the generated position at (0,0,0), as illustrated in Fig. 13. Note that this 33% inefficiency includes cases where no vertex is found. This is significantly worse than the vertexing efficiency for muon-proton events (90%) due to the fact that hits from the shower can distract the principal curve algorithm from

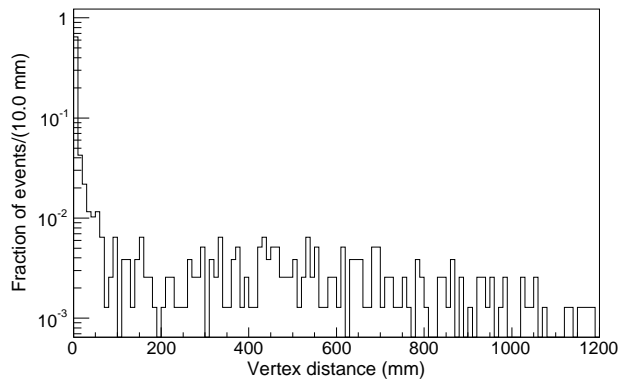


Fig. 13 The distribution of the distance of the reconstructed primary vertex position from the generated position (0,0,0) for electron-proton events that pass the range selection on the proton track

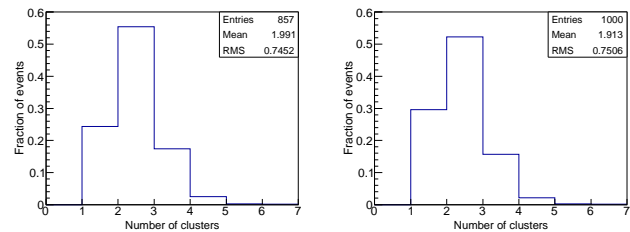


Fig. 14 The distribution of reconstructed clusters in a sample of 1000 electron-proton events for (left) events passing a range selection on the proton track and (right) with no range requirement imposed

picking up the proton track. Indeed, the random nature of the hit positions in the shower can induce multiple feature points to be found along the principal curve. Figure 14 shows the number of reconstructed clusters for the sample of electron-proton events with and without the proton hit selection requirement. Most events have two clusters reconstructed, as expected, although for about 25% of the selected events, or 30% in the full sample, the proton track has not been found. Approximately 20% of the remaining events have more than two clusters found, meaning that a primary vertex (with the lowest x co-ordinate) has been reconstructed together with secondary vertices embedded inside the electron shower. This is about a factor of two higher than the number of multiple vertices found for muon-proton events, despite including the requirement that neighbouring clusters are merged, and the vertex between them removed, if the angle between their principal axes is less than 20 degrees.

As was done for the muon-proton sample, the parameters of the principal curve defined in Table 1 were optimised in order to give, on average, two clusters per electron-proton event, as well as providing maximal

Table 4 Optimised performance of the lpc algorithm for 770 MeV neutrino to electron-proton events that satisfy the proton range requirement (857 out of an initial sample of 1000). Efficiencies and purities are averaged over all selected events

Quantity	Value
Lpc scaled kernel bandwidth h	0.072
Lpc scaled step size t	0.040
Number of lpc points	100
Fraction of events with no vertex found	24.4 ± 1.5 %
Electron cluster efficiency	99.6 ± 0.2 %
Electron hit efficiency	74.5 ± 1.5 %
Electron reconstruction efficiency	74.3 ± 1.5 %
Electron hit purity	97.5 ± 0.5 %
Electron shower efficiency	93.4 ± 0.6 %
Proton cluster efficiency	63.9 ± 1.6 %
Proton hit efficiency	92.8 ± 0.9 %
Proton reconstruction efficiency	59.3 ± 1.7 %
Proton hit purity	96.8 ± 0.6 %
Proton shower efficiency	11.9 ± 0.7 %
Vertex efficiency within ± 2 cm	67.3 ± 0.9 %
Vertex x position resolution	1.52 ± 0.09 mm
Vertex y position resolution	1.62 ± 0.09 mm
Vertex z position resolution	1.62 ± 0.10 mm

cluster and hit efficiencies and purities for the reconstructed electron and proton clusters. Again, the most important parameters are the kernel width h , the step size t and the number of lpc points N_p . Table 4 shows the results from this optimisation, including the average efficiencies of identifying the electron and proton clusters as showers, $93.4 \pm 0.6\%$ and $11.9 \pm 0.7\%$ respectively, using the procedure described in Sect. 5. Note that the efficiency of reconstructing the proton cluster is strongly dependent on the efficiency of finding a primary vertex. It was found that variations to the step size within the range 0.04 to 0.06 did not significantly affect the reconstruction performance, provided the kernel-to-step size ratio was kept near values between 1.6 and 1.8. Additionally, using between 100 and 300 lpc points produced similar results.

Despite most of the electrons being correctly found and identified as showers, about 25% of their hits are not included in the (main) cluster. Some of these missing hits are at the outer edge of the shower hit cloud, with δr residuals larger than 10 cm. However, most of them are misclassified as a separate cluster within the main shower, which happens if more than one vertex has been reconstructed. This will have a direct effect on the reconstructed energy of the electron cluster, which is simply taken to be the sum of the energy deposits Q_i of all of the associated hits. Figure 15 shows the generated quenched energy distributions for electrons and protons (770 MeV ν_e events), as well as the reconstructed energies of the electron and proton clusters when most of their hits have the correct particle

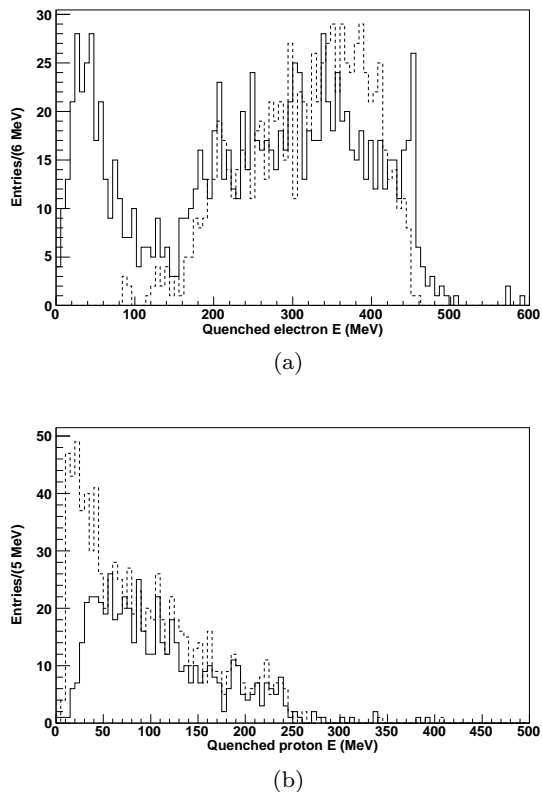
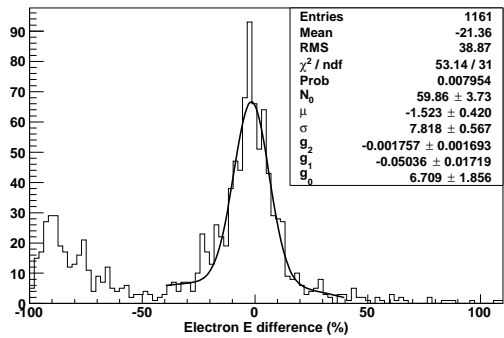
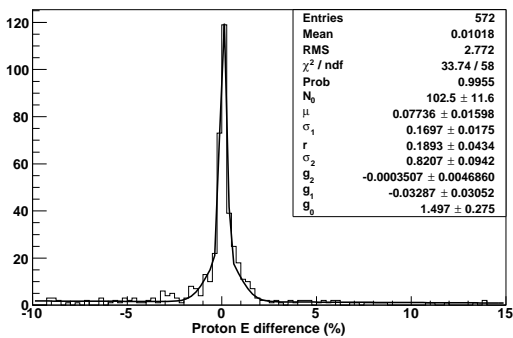


Fig. 15 Plots (a) and (b) show the reconstructed (solid line) and generated (dotted line) quenched energy histograms for the electrons and protons in 770 MeV $\nu_e + n \rightarrow e + p$ events

type. We can see that there is a secondary peak below 100 MeV for the electron distribution, corresponding to the missing hits in the main cluster. Furthermore, most of the protons that are not reconstructed have generated (quenched) energies below 50 MeV; the hits from these protons are instead associated to the main electron cluster, leading to reconstructed energies that are higher than the generated values. Figure 16 shows the distributions of the fractional energy difference $f_E = (E_{\text{reco}} - E_{\text{gen}})/E_{\text{gen}}$, where E_{reco} is the reconstructed cluster energy and E_{gen} is the generated particle energy. The f_E distribution for electrons has a main single-Gaussian peak with a width corresponding to a quenched energy resolution of approximately 8%. The secondary peak occurs for f_E values below -50% , and corresponds to additional clusters found inside the electron shower. The f_E distribution for correctly identified protons has a very narrow peak, which is to be expected since the proton hit efficiency and purity are both above 92%. Fitting a double Gaussian function (common mean, two widths) to this peak gives an effective quenched energy resolution approximately equal to 0.3% for protons. This compares well to the



(a)

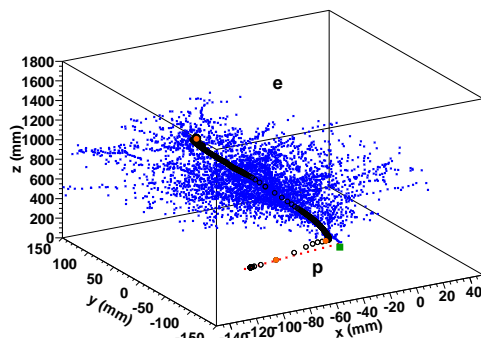


(b)

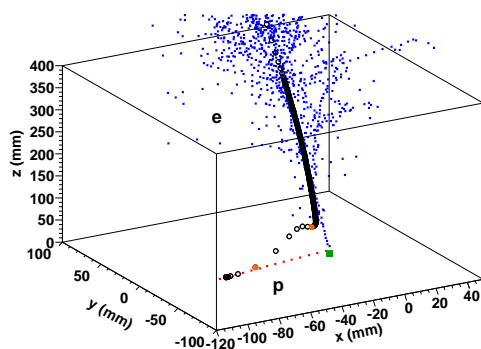
Fig. 16 Distributions of the fractional difference f_E between the generated and reconstructed quenched energies for (a) electrons and (b) protons shown in Fig. 15. The main peak of the electron (proton) distribution is fitted with a single (double) Gaussian with a quadratic polynomial background $g_2 f_E^2 + g_1 f_E + g_0$. The height of each Gaussian function is given by N_0 , while μ and σ denote the mean and width, respectively. The relative normalisation between the two Gaussian terms (same mean, different widths σ_1 and σ_2) for the proton fit is given by the parameter r

effective energy resolution of approximately 0.2% for the reconstructed clusters in the previously mentioned muon-proton sample.

So far we have only looked at low-energy (< 1 GeV) neutrino interactions. Figure 17 shows the lpc reconstruction of a high energy (~ 9 GeV) electron-proton event. The electron shower extends over a very wide area, which means that the number of points in the principal curve needs to be significantly increased from around 100 to at least 500 in order to cover most of the core region of the shower, following the hits along the principal axis. Additionally, the scaled kernel width needs to be increased to the value 0.11 for a step size of 0.06. A close-up view of the event near the primary vertex region shows that the start of the electron shower is almost track-like, as was observed for the lower energy electrons. In this region, the principal curve starts to move away from the electron hits towards the proton



(a)



(b)

Fig. 17 The lpc reconstruction of a high energy electron-proton event showing the hits associated to the 9.0 GeV electron shower (blue) and 0.1 GeV proton track (red) together with the calculated lpc points (open circles). Also shown are the feature points of the principal curve (orange-filled circles) and the reconstructed primary interaction vertex (green square). Plot (b) is a close-up view of the interaction region of plot (a)

track. During this transition, the sheer number of hits in the shower start to push the principal curve back towards itself. However, the local nature of the algorithm forces the points back onto the proton track. This push-and-pull effect creates two feature points which are actually close enough to create a merged range of lpc points that are used for finding the primary vertex location via the extended straight line method described in Sect. 4. Inside the electron shower, there is an additional feature point near the end of the principal curve, owing to the rather wide spread of hits at the edge of the shower affecting the convergence of the curve, producing large angles between the remaining eigenvectors.

In most high-energy events, the algorithm finds multiple feature points inside the core of the shower which adversely affects the performance of correctly finding the primary vertex location, especially if the proton

track has a very small range and is not well separated from the shower. In order to consistently reconstruct high-energy events correctly, other tools and methods need to be developed and incorporated into the lpc algorithm.

7 Conclusion

We have presented a local principal curve algorithm that can reconstruct neutrino interaction events in liquid argon. The algorithm creates a series of (three-dimensional) points that follows the local density of hits. It does so by calculating the localised mean shift, which changes direction based on the largest eigenvector obtained from the 3×3 covariance matrix of a set of weights which determine the size and shape of the local neighbourhood of points. Differences in the angle ϕ between consecutive eigenvectors can produce peaks in the $1 - |\cos\phi|$ distribution when the principal curve is rapidly changing direction. These peaks correspond to feature points which highlight the presence of interaction vertices, which can be reconstructed by finding the point of closest approach between two straight line sections associated to nearby hits on either side of a given feature point. Clusters can then be formed by continuing along the principal curve direction initially given by each straight line section and adding hits that are closest to the remaining lpc points. The residual distance between hits and their nearest lpc point, together with a measure of the size of a convex hull encompassing all of the hits in a cluster, can be used to discriminate showers from tracks. The reconstruction performance of the algorithm with regards to vertexing, clustering, energy resolution and track-shower identification has been tested on 770 MeV neutrino interaction muon-proton (CCQE) and electron-proton events. For high-energy events, further work is required to better use the information provided by the increased number of feature points.

There are possible further uses of this algorithm. For example, it is straightforward to use it to identify clusters when the hit positions are only known in two dimensions; the third co-ordinate for all hits is just set to zero or ignored, and all other procedures remain the same. Additionally, it should be possible to use the algorithm to find feature points and reconstruct clusters for events when more than two particles originate from a common vertex point. Here, points along the principal curve will only be able to follow the two main particles which will contain the majority of the hits. To find the other particles, the hits associated to the two reconstructed clusters need to be removed and the algorithm re-run on the remaining hits. However, care must be

taken to avoid removing hits unnecessarily within such a procedure. A possible way to proceed is to use the ratio between the first and second largest eigenvalues of the covariance matrix defined in Eq. 5, which may indicate the presence of bifurcation (“branching”) points that can act as starting locations for further principal curves. At the time of writing, we have not yet studied a strategy for reconstructing multi-particle final state interactions.

To conclude, the local principal curve algorithm provides a wealth of information that can be used to automatically reconstruct neutrino interaction events in liquid argon detectors.

Acknowledgements We thank Daniel Brunt, Harmanjeet Khera and Jamie Wynn who all worked with the group as part of the University of Warwick project student programme. This work was financially supported by the Science and Technology Facilities Council consolidated grant ST/H00369X/1 and by the European Community under the European Commission Framework Programme 7 grant LAGUNA-LBNO/FP7-INFRASTRUCTURES/284518.

References

1. A. Rubbia, J. Phys. Conf. Ser. **308**, 012030 (2011)
2. C. Rubbia et al. (ICARUS Collaboration), J. Instrum. **6**, P07011 (2011)
3. J. Einbeck, G. Tutz, L. Evers, Stat. Comput. **15**, 301 (2005)
4. D. Comaniciu, P. Meer, IEEE Trans. Pattern Anal. Mach. Intell. **24**, 603 (2002)
5. M. Zayed, Curve estimation based on localized principal components – theory and applications, PhD thesis, Durham University (2011)
6. J. Einbeck, L. Evers, K. Hinchliff, in *Advances in Data Analysis, Data Handling, and Business Intelligence*, ed. by A. Fink, B. Lausen, W. Seidel, A. Ultsch (Springer, Heidelberg, 2010), p. 701
7. S. Agostinelli et al., Nucl. Instrum. Methods A **506**, 250 (2003)
8. S. Amoroso et al., Nucl. Instrum. Methods A **523**, 275 (2004)
9. C. Andreopoulos, Nucl. Instrum. Methods A **614**, 87 (2010)
10. M. Ester, H.P. Kriegel, S. Joerg, X. Xu, in *Proceedings of the 2nd International Conference on Knowledge Discovery and Data Mining*, Portland, 1996, ed. by E. Simoudis, J. Han, U.M. Fayyad (AAAI Press, 1996), p. 226
11. M. Daszykowski, B. Walczak, D.L. Massart, Chemom. Intell. Lab. Syst. **56**, 83 (2001)
12. C.B. Barber, D.P. Dobkin and H.T. Huhdanpaa, ACM Trans. Math. Softw. **22**, 469 (1996)